



Computations of incompressible fluid flow around a long square obstacle near a wall: laminar forced flow and thermal characteristics

DEEPAK KUMAR and AMIT KUMAR DHIMAN*

Department of Chemical Engineering, Indian Institute of Technology Roorkee, Roorkee 247 667, India
e-mail: dhimuamit@rediffmail.com; amitdfch@iitr.ac.in

MS received 5 May 2016; revised 10 November 2016; accepted 6 December 2016

Abstract. Computations of incompressible fluid flow and heat transfer around a square obstacle with a nearby adiabatic wall have been performed in a horizontal plane. The ranges of dimensionless control parameters considered are Prandtl number (Pr) = 10–100, Reynolds number (Re) = 1–150 and gap ratio (G) = 0.25–1. The steady-flow regime is observed up to $Re = 121$ for $G = 0.5$, and beyond this Re , time-periodic regime is observed. The shift to a time-periodic regime from a steady regime occurred at greater Re than that for an unconfined square obstacle. With increasing Pr , increase in average Nusselt number values is recorded for all Re and G studied. The heat transfer augmentation is approximately 1332% at $Re = 150$ ($Pr = 100$, $G = 0.25$) with regard to the corresponding values at $Re = 1$. Lastly, a correlation for j_h factor is determined for the preceded conditions.

Keywords. Square obstacle; shear flow; drag and lift coefficients; Strouhal number; average Nusselt number; heat transfer enhancement.

1. Introduction

Incompressible Newtonian fluids flow and heat transfer around a square obstacle are typical problems in fluid mechanics and are widely encountered in several engineering appliances, for instance, novel heat exchangers, evaluation of hydrodynamic forces exerted on various pipelines, probes/sensors and so forth. Additionally, the neighbourhood of a wall can have noticeable impacts on the flow and heat transfer attributes near an obstacle. Also, the interference between the wall and the obstacle directed towards the variations in both steady and unsteady forces act on the obstacle. Therefore, the current work is related to the forced flow and heat transfer from a long square obstacle close to a wall in the laminar regime. The flow over a square obstacle in close proximity to a wall is characterised by the flow control parameters (e.g. incoming fluid velocity and Reynolds number (Re)), thermal control parameters (e.g. fluid temperature and Prandtl number (Pr)) and physical dimensions (e.g. sides of a square obstacle (D) and gap ratio (G); i.e. the ratio between the gap of a square obstacle and the channel wall to the side of the square). It is also valuable to point out that the flow around a square obstacle in the neighbourhood of a wall is more complex than the free-stream square obstacle because of the interaction of the square obstacle and wall shear layers, and limited information available in the literature [1]. On

the contrary, extensive literature is reported on a circular obstacle in the neighbourhood of a wall. Thus, it is advantageous to analyse pertinent studies on square and/or circular cross-section obstacles.

For a circular obstacle in the propinquity of a wall, the vortex shedding is examined for different gap heights (0.3–3) as well as Re varying from 80 to 1000 [2]. The vortex shedding mechanism at low gap spacing was evaluated, and the critical gap spacing was found to be 0.6, 0.78, 1 and 1.2 for $Re = 200$, 150, 100 and 78, respectively. The onset of periodicity is computed for a confined circular obstacle for $Re \leq 1800$ and $G \leq 2$ [3]. Shifting to a time-periodic state from a steady state has been deferred as the cylinder reaches the wall. For $G = 2$, the transition is between $Re = 230$ and 240. As the gap is decreased to 0.25, there is a fast growth in the critical Re and finally the transition arises between $Re = 1500$ and 1800. The effect of thermal conductivity is studied for a cylinder in the propinquity of wall for $Re = 0.001$ –1 and $G = 0.1$ –10 [4]. Low-conductivity wall materials (e.g. mirror, glass and perspex) have a leading impact on the heat transfer from the obstacle in the proximity of a wall. As G decreased from 5 to 0.7 at $Re = 180$, Strouhal number (St) rises to a maximum at a gap ratio of 0.7 [5–7]. Further gap reduction from 0.7 to 0.1 leads to a rapid decrease in St , with shedding finally ceasing altogether at gap ratios below 0.16. The heat transfer and fluid flow behaviours are studied for $Re = 20$ –200 and $G = 0.1$ –2.5 at $Pr = 0.7$ in [8]. The vortex shedding is entirely eliminated when the obstacle is

*For correspondence

positioned below critical gap spacing. Unlike preceded studies, the two-dimensional (2-D) flow around a rotating circular obstacle in the neighbourhood of a wall is simulated for $G = 0-5$ at a fixed $Re = 200$ [9]. Two critical values of G (e.g. G_{down} and G_{up}) were found, which rely on the rotational rate ($G_{down} = 0.4$ and $G_{up} = 1.5$ for rotational rate = 0.5, and $G_{down} = 0.6$ and $G_{up} = 1.5$ for rotational rate = 1). Also, rotating circular cylinders in close proximity to a wall ($G = 0.005$) were studied for $Re = 20-750$ [10]. It was observed that the cylinder rolling backward can entirely eliminate the vortex shedding. The variations of wake dynamics and turbulence characteristics in the neighbourhood of a wall for $G = 0.25-1$ were observed in [11] and also illustrated the physics comprising the shear layer transition, stretching, breakdown and turbulence production for $Re = 1440$.

The separation points on a square obstacle are generally placed at the corner points and, as a result, exert significant influences on flow and heat transfer features. The presence of a wall in the neighbourhood of a square obstacle was studied numerically in [12–24] and the detailed discussion on the literature is now available in our recent work [1]. The two- and three-dimensional (3-D) effects were investigated on a square cylinder located at $G = 0.2-4$ for $Re = 175, 185$ and 250 [16]. At $Re = 175$ and 185 , a slight difference was observed for 2-D and 3-D simulations but a significant variation was observed at $Re = 250$. The effect of forced convection heat transfer using turbulent flow model at $Re = 10-50,000$ was studied for $G = 0.25-3$ and air as a working fluid [18]. Critical points were recorded for which the transition between oscillatory flow and steady flow occurs. Furthermore, experimental practices on the flow past a square obstacle in the neighbourhood of a wall were performed at high Re [19–24].

Thus, the aforementioned discussion suggests that the majority of the prior experimental/numerical observations focused on vortex shedding from the square and/or circular obstacles for laminar and/or turbulent regime at high Re . A study [12] deals with the shear flow near a plane wall for

$G = 0.25, 0.5$ and $Re = 100, 125, 400$. However, studies [1, 14, 15, 18] deal with flow and heat transfer aspects close to a plane wall taking air ($Pr = 0.7$) as a working fluid. Furthermore, it is to be noted that uniform inlet velocity is assumed in previous studies [15, 18] and the heat transfer is studied for $Re = 100-250$ at a fixed $G = 0.5$ in another study [14]. Our recent work [1] is limited to the mixed convection heat transfer results for $Pr = 0.7$ and Re up to 100 at Richardson number (Ri) = 0 to 1 and $G = 0.25$ to 1. However, in the current study, effects of Pr are investigated for the wider range of settings as opposed to our recent work [1]. The numerical methodology has also been validated extensively with literature [12, 14, 25–31]. Specifically, the novelty of the present work can be realised based on the following important issues:

- No heat-transfer observations for high Pr (>0.7) near a plane wall are available in the literature.
- The onset of vortex shedding (i.e. the shifting of unsteady periodic regime from a steady regime) is not yet explored for $G = 0.5$.

Thus, in the present study, an effort has been made to address these issues.

2. Problem description

The laminar flow and heat transfer have been considered in the horizontal plane for Newtonian fluids around a long square cylinder (long in neutral direction) in the proximity of an adiabatic wall (figure 1). At inlet, the incompressible fluid is coming with a linear velocity and having a constant temperature of T_∞ ; however, the square obstacle temperature is maintained constant at T_w such that $T_w > T_\infty$. The dimensionless upstream (L_u) and downstream (L_d) dimensions and the domain height (H) are 15, 50 and 20, respectively. These dimensions have been chosen after domain independence study, which is thoroughly discussed in section 3.

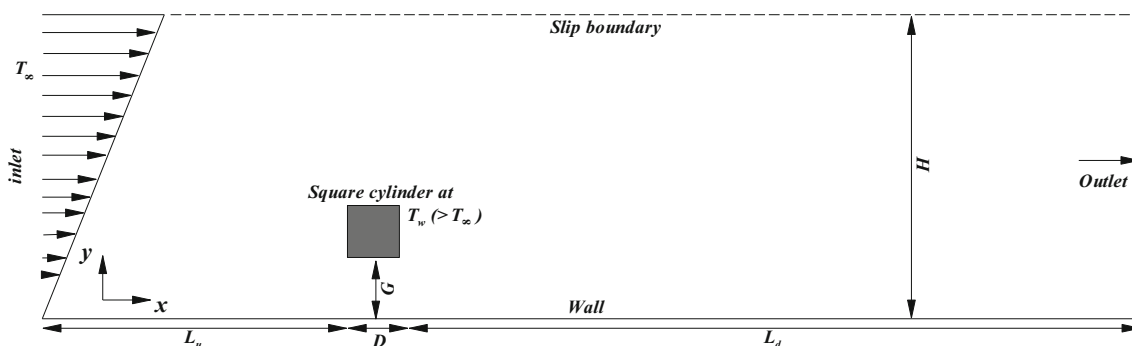


Figure 1. Schematic diagram.

Table 1. Grid dependence study for $N = 60\text{--}140$ CVs at $Re = 150$, $G = 0.25$ and $Pr = 100$.

Grid size Output parameters	48,528 cells		68,300 cells N = 100 CVs	90,320 cells	
	N = 60 CVs	% variation between N = 60 CVs and N = 100 CVs		N = 140 CVs	% variation between N = 140 CVs and N = 100 CVs
C_L	1.4278	0.02	1.4275	1.4274	0.01
C_D	2.6564	0.01	2.6561	2.656	0.00
\overline{Nu}	32.2997	0.95	31.9953	31.7749	0.69

Table 2. Grid dependence study for $\delta = 0.005D - 0.01D$ at $Re = 150$, $G = 0.25$ and $Pr = 100$.

Grid size Output parameters	78,504 cells		68,300 cells $\delta = 0.008D$	65,198 cells	
	$\delta = 0.005D$	% variation between $\delta = 0.005D$ and $\delta = 0.008D$		$\delta = 0.01D$	% variation between $\delta = 0.01D$ and $\delta = 0.008D$
C_L	1.4319	0.31	1.4275	1.4251	0.17
C_D	2.6595	0.13	2.6561	2.6547	0.05
\overline{Nu}	31.5599	1.36	31.9953	32.1697	0.55

The incoming fluid is assumed to be having constant fluid properties [1]. Also, the viscous dissipation term in the thermal energy equation is ignored. Additionally, the value of Richardson number is calculated using the data available in the literature [30] and it has been found that the value of Richardson number is changing here from 0.014 to 0.066 for the working fluids considered. Owing to such low values of Richardson numbers, the buoyancy effects are very weak and the forced convection mode is predominant. Hence, the impact of the mixed convection is neglected in this investigation. Thus, the continuity (Eq. 1), the components of momentum (Eqs. 2 and 3) and the energy (Eq. 4) equations in the dimensionless form for the present framework are given as

$$\frac{\partial u}{\partial x} + \frac{\partial v}{\partial y} = 0 \quad (1)$$

$$\frac{\partial u}{\partial t} + \frac{\partial uu}{\partial x} + \frac{\partial vu}{\partial y} = -\frac{\partial p}{\partial x} + \frac{1}{Re} \left(\frac{\partial^2 u}{\partial x^2} + \frac{\partial^2 u}{\partial y^2} \right) \quad (2)$$

$$\frac{\partial v}{\partial t} + \frac{\partial uv}{\partial x} + \frac{\partial vv}{\partial y} = -\frac{\partial p}{\partial y} + \frac{1}{Re} \left(\frac{\partial^2 v}{\partial x^2} + \frac{\partial^2 v}{\partial y^2} \right) \quad (3)$$

$$\frac{\partial \theta}{\partial t} + \frac{\partial u\theta}{\partial x} + \frac{\partial v\theta}{\partial y} = \frac{1}{Re Pr} \left(\frac{\partial^2 \theta}{\partial x^2} + \frac{\partial^2 \theta}{\partial y^2} \right) \quad (4)$$

The boundary settings (in non-dimensional form) can be noted as follows: At the inlet: $u = y$, $v = 0$ and $\theta = 0$, where the slope is unity [1, 12–14]. On the top domain side: $\partial u/\partial y = 0$, $v = 0$ and $\partial \theta/\partial y = 0$ [1, 12–14]. On the bottom domain side: $u = 0$, $v = 0$ and $\partial \theta/\partial y = 0$. On a square obstacle: $u = 0$, $v = 0$ and $\theta = 1$. At the downstream outlet: it is placed adequately distant from the square

obstacle and a zero normal velocity/temperature gradient is applied such that $\partial u/\partial x = 0$, $\partial v/\partial x = 0$ and $\partial \theta/\partial x = 0$. Equations (1)–(4) with boundary conditions are solved by adopting Ansys Fluent [31] and the computational grid is constructed by making use of Ansys workbench. More numerical details about grid structure, discretisation schemes, numerical method to solve algebraic equations and convergence criteria can be found in a study by Kumar and Dhiman [1].

3. Grid, domain and time independence studies

Because this study covers the wider ranges of $Pr (>0.7)$ and Re (up to 150) than that of Kumar and Dhiman [1], then the new details on the grid, domain and time independence studies are discussed as follows:

In this work, grids consisting of 68,300, 80,000 and 122,000 cells for $G = 0.25, 0.5$ and 1 respectively are used. To justify these choices of grid sizes, the grid size is examined by monitoring the engineering output control parameters; the grid dimensions of 48,528, 68,300 and 90,320 cells are applied with $N = 60, 100$ and 140 CVs on each side of the square obstacle, respectively. The calculations are performed for the severe values of $Re (=150)$, $Pr (=100)$ and $G (=0.25)$. The maximum differences in the values of dimensionless flow and heat transfer output values, for instance, drag coefficient (C_D), lift coefficient (C_L) and Nusselt number (\overline{Nu}) for the cases of $N = 60$ CVs with respect to $N = 100$ CVs are found to be less than 1% (table 1). The corresponding maximum differences for $N = 140$ CVs with respect to $N = 100$ CVs are found to be only $\sim 0.7\%$. Thus, the grid size of 68,300 cells with

Table 3. Upstream dependence study for $Re = 1, 150$ and $Pr = 100$ at $G = 0.25$.

Grid size	66,694 cells		68,300 cells	72,128 cells	
	$L_u = 10D$	% variation between $L_u = 10D$ and $L_u = 15D$		$L_u = 20D$	% variation between $L_u = 20D$ and $L_u = 15D$
Output parameters					
$Re = 1$					
C_L	5.958	0.84	5.9088	5.9264	0.30
C_D	24.6255	0.53	24.4959	24.5527	0.23
\overline{Nu}	2.238	0.17	2.2343	2.2358	0.07
$Re = 150$					
C_L	1.4576	2.11	1.4275	1.4167	0.76
C_D	2.7114	2.08	2.6561	2.6365	0.74
\overline{Nu}	32.5552	1.75	31.9953	31.7574	0.74

Table 4. Downstream dependence study at $Re = 150, G = 0.25$ and $Pr = 100$.

Grid size	65,429 cells		68,300 cells	71,432 cells	
	$L_d = 40D$	% variation between $L_d = 40D$ and $L_d = 50D$		$L_d = 50D$	% variation between $L_d = 60D$ and $L_d = 50D$
Output parameters					
C_L	1.4275	0	1.4275	1.4275	0
C_D	2.6561	0	2.6561	2.6561	0
\overline{Nu}	31.9961	0	31.9953	31.9969	0.01

Table 5. Domain height dependence study for $Re = 1, 150$ and $Pr = 100$ at $G = 0.25$.

Grid size	52,100 cells		68,300 cells	84,500 cells	
	$H = 10D$	% variation between $H = 10D$ and $H = 20D$		$H = 20D$	% variation between $H = 20D$ and $H = 30D$
Output parameters					
$Re = 1$					
C_L	6.5819	11.39	5.9088	5.8492	1.01
C_D	27.0685	10.5	24.4959	24.2561	0.98
\overline{Nu}	2.3007	2.97	2.2343	2.2280	0.28
$Re = 150$					
C_L	1.4661	2.70	1.4275	1.4231	0.31
C_D	2.7359	3.00	2.6561	2.6471	0.34
\overline{Nu}	32.2804	0.89	31.9953	32.005	0.03

$N = 100$ CVs is utilised (table 1). Also, the consequences of change of the smallest cell dimension (δ) near the square cylinder on the output parameters are examined and the outcomes are tabulated in table 2. The results at $\delta = 0.008D$ are found to lie between the results for $\delta = 0.005D$ and $0.01D$. For instance, the maximum relative change for $\delta = 0.005D$ with respect to $\delta = 0.008D$ is found to be less than 1.4%. Thus, the dimensionless grid spacing of 0.008 close to the square obstacle is used for further simulations.

The influence on the flow and heat transfer output values is examined for the upstream length (L_u) = 10D (66,694

Table 6. Time dependence study for $Re = 150$ and $Pr = 100$ at $G = 0.25$ and 1.

Output parameters	$\Delta t = 0.0075$	$\Delta t = 0.01$	$\Delta t = 0.0125$
$G = 0.25$			
C_L	1.4275	1.4275	1.4275
C_D	2.6561	2.6561	2.6561
\overline{Nu}	32.0259	31.9953	31.9981
$G = 1$			
C_L	0.1457	0.1419	0.1431
C_D	4.897	4.897	4.8985
\overline{Nu}	41.1673	41.1718	41.1659

Table 7. Validation of present results with Bhattacharyya *et al.* [14] at different values of Re for $G = 0.5$ and $Pr = 0.7$.

Re	Bhattacharyya <i>et al.</i> [14]	Present work
100	$C_L = 0.8256$	0.8687
125	$C_L = 0.7143$	0.7350
	$C_D = 3.4192$	3.2388

cells), $15D$ (68,300 cells) and $20D$ (72,128 cells) for both end values of Re (1 and 150) at $Pr = 100$, $G = 0.25$ and is documented in table 3. Table 3 also records the percentage relative deviations with $L_u = 15D$. From table 3, the relative maximum differences for these parameters are noted higher for $L_u = 10D$ with $L_u = 15D$, and the changes are noted lesser for $L_u = 20D$ with $L_u = 15D$. Therefore, a dimensionless upstream length of 15 is employed. On the other

hand, the impact of the downstream length (L_d) is studied for three downstream lengths of $40D$ (65,429 cells), $50D$ (68,300 cells) and $60D$ (71,432 cells) at $Re = 150$, $Pr = 100$ and $G = 0.25$ (table 4). It is recorded that the values of C_D , C_L and \overline{Nu} are independent of the downstream distances, and hence a dimensionless downstream distance of 50 is utilised.

The influence on the values of output parameters is investigated for the height of the computational field (H) = $10D$ (52,100 cells), $20D$ (68,300 cells) and $30D$ (84,500 cells) for both end values of Re (1 and 150) at $Pr = 100$, $G = 0.25$ (table 5). Table 5 also records the percentage relative deviations with $H = 20D$. The relative maximum differences for these parameters are noted higher for $H = 10D$ with $H = 20D$, and the changes are noted fewer for $H = 30D$ with $H = 20D$. Hence, a dimensionless domain height of 20 has been used for further studies.

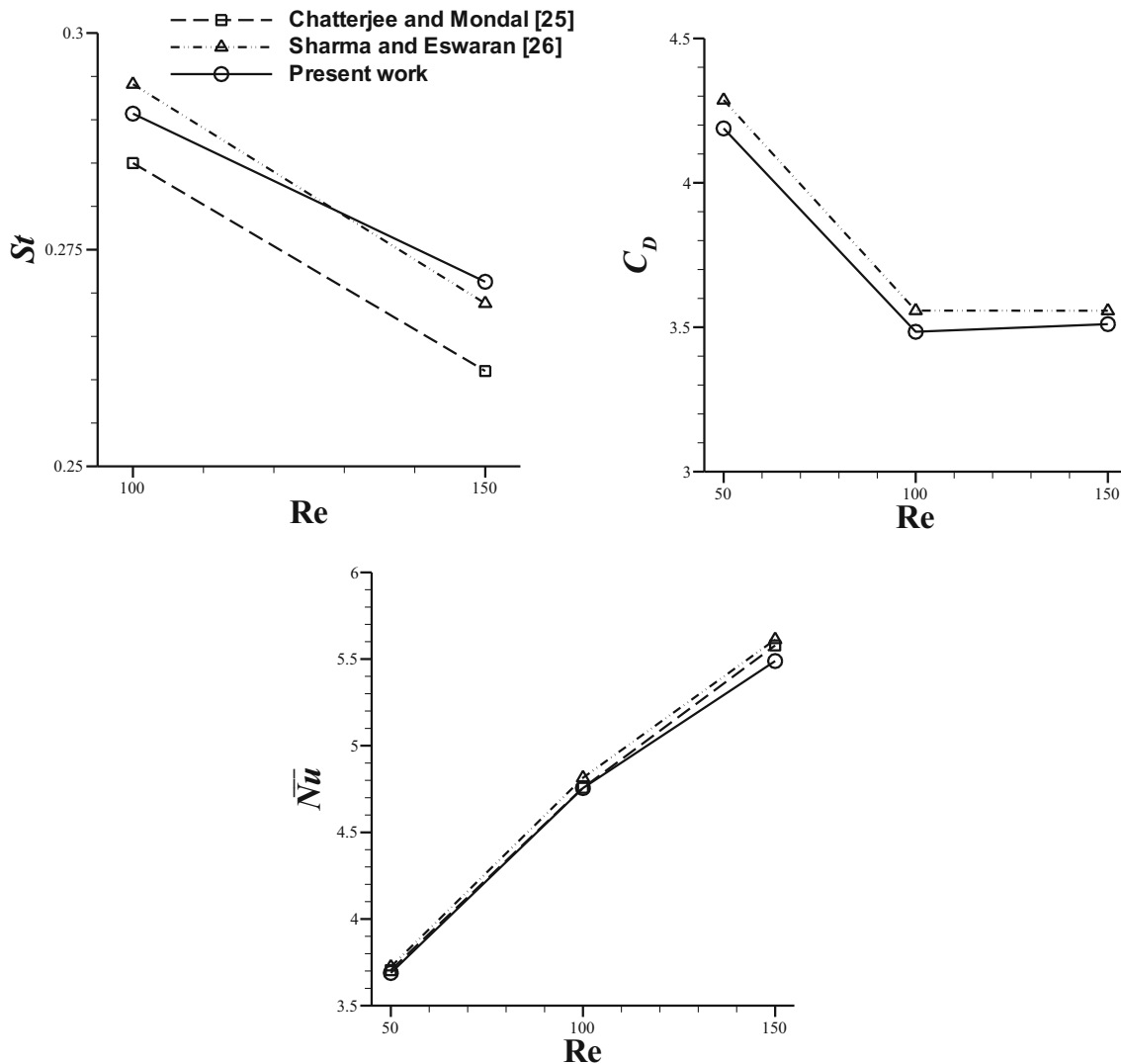


Figure 2. Benchmarking of results with literature [25, 26].

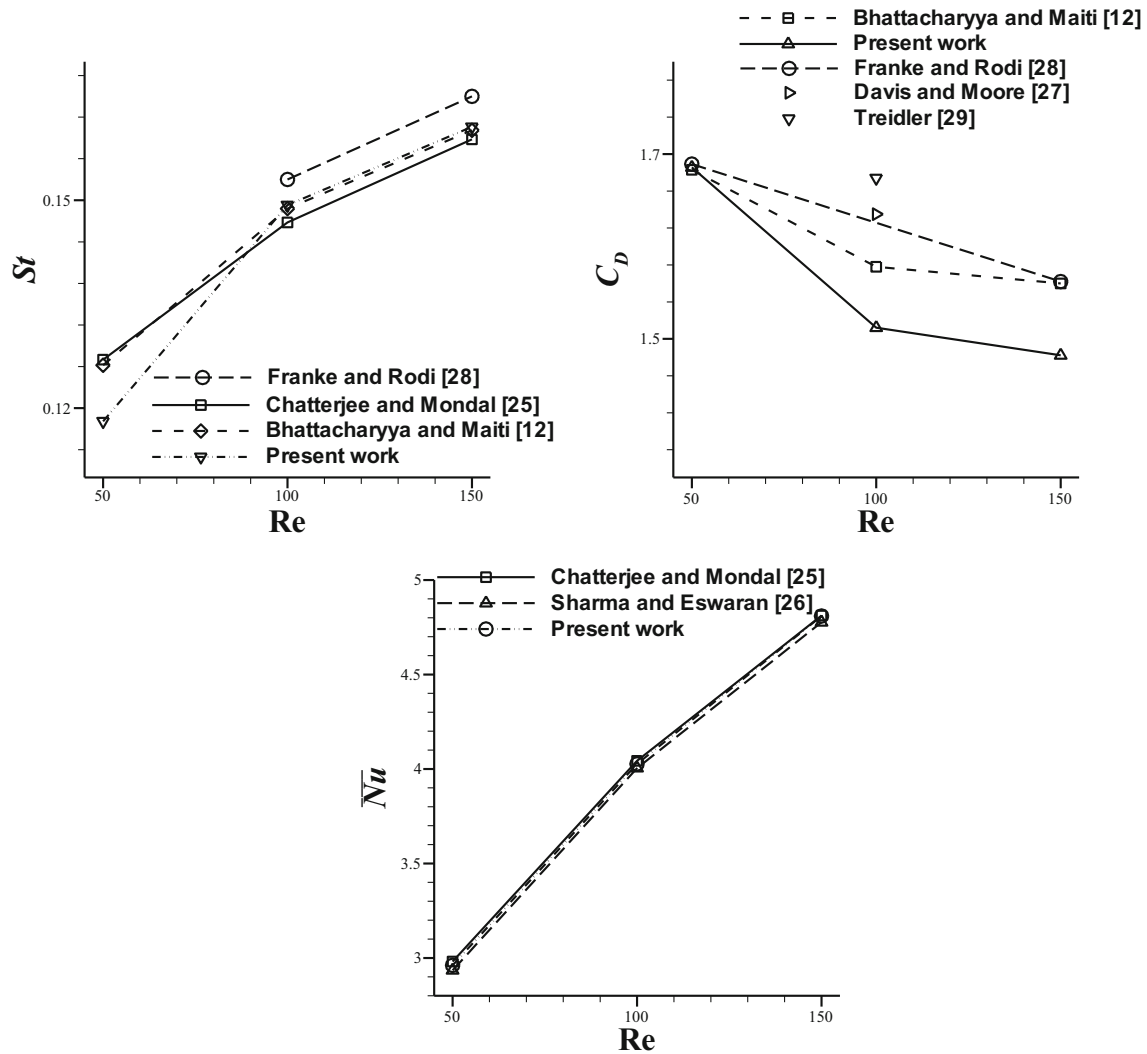


Figure 3. Validation of results with experimental/numerical values [12, 25–29].

The effect of time step (Δt) on output parameters has also been investigated for $\Delta t = 0.0075, 0.01$ and 0.0125 at $Pr = 100, G = 0.25, 1$ and $Re = 150$ (table 6). The maximum relative variations in the values of average Nusselt number are noted around 0.1% at $G = 0.25$; however, no variation is noted for C_D and C_L . Similarly, the time-dependence test is performed for time-periodic case at $G = 1$ for $Pr = 100$ and $Re = 150$ (table 6). The maximum relative deviations in the values of the parameters for $\Delta t = 0.0075$ with respect to $\Delta t = 0.01$ are found to be $\sim 2.7\%$, and for $\Delta t = 0.0125$ with respect to $\Delta t = 0.01$ the changes are found to be only $\sim 0.8\%$. It can be observed here that $\Delta t = 0.0075$ is not sufficient because the results, when compared with $\Delta t = 0.01$, vary significantly. However, when $\Delta t = 0.01$ is compared with an even larger time step ($\Delta t = 0.0125$), the insignificant deviation in the results has been noticed. Hence, a

dimensionless time step of 0.01 has been used, which is also sufficient to resolve the unsteady cases.

4. Results and discussion

The flow and heat transfer results for $Pr = 10$ – 100 at $Re = 1$ – 150 and $G = 0.25$ – 1 are presented and discussed. Mahir [16] performed the 2-D and 3-D numerical simulations to investigate the effect of flow features around a square cylinder near a plane wall. He performed computations for gap ratios of 0.2–4 and $Re = 175, 185$ and 250. At $Re = 175$ and 185, a slight difference is observed for 2-D and 3-D simulations but a major difference is observed at 250. Therefore, the 2-D assumption in the present work is believed to be justified. However, before discussing the

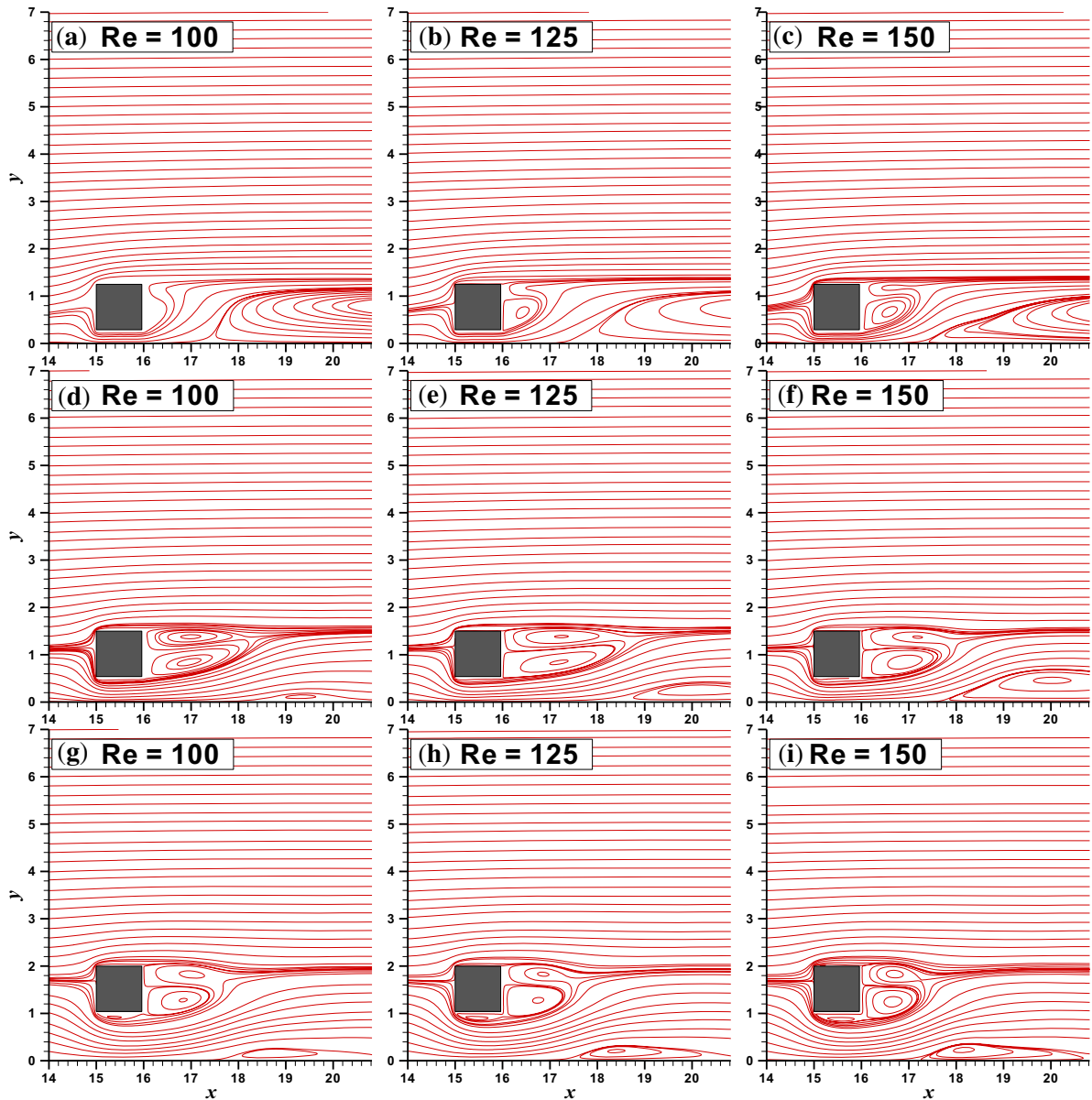


Figure 4. Time-averaged streamlines for (a–c) $G = 0.25$, (d–f) $G = 0.5$ and (g–i) $G = 1$.

new results, the present methodology has been validated thoroughly with literature [12, 14, 25–31] in section 4.1.

4.1 Validation

First, the validation of the current work is completed with the results available in [14]. For this, the time-dependent fluid flow and heat transfer investigations were conducted for $Re = 100$ and 125 at $G = 0.5$ and $Pr = 0.7$ (table 7). At $Re = 100$, it has been noted that the present C_L differs by $\sim 5.2\%$ compared to previous

study [14]. At $Re = 125$, the present values of flow quantities like C_D and C_L have the maximum deviations of $\sim 5.3\%$ and 2.9% , respectively. The slightly larger differences in the flow output parameter values between two studies are attributed to the fact that an upstream distance of 8, downstream distance of 40, coarse grid size of 31,450 cells, implicit first-order scheme and residual of 0.5×10^{-4} were used in a study [14], but in the current work an upstream distance of 15, downstream distance of 50, fine grid size of 68,300 cells, implicit second-order scheme and residual of 10^{-15} are being used.

Secondly, to gain confidence on the numerical methodology used, we have further compared various output flow parameters with reliable experimental/numerical values for confined/unconfined configurations. In a confined domain, the present results for the flow past a square obstacle, with a parabolic velocity profile at the inlet, for Prandtl number of 0.7 and blockage ratio of 25% at various values of Re are compared in figure 2 with literature [25, 26]. The difference amongst the values of C_D , St and \overline{Nu} of the current study with that of literature [25, 26] is achieved less than 2%. Therefore, the present analysis has an excellent agreement with literature [25, 26]. Also, the present results for the case of unconfined flow across a square obstacle are evaluated and presented in figure 3 with literature [12, 25–29] for the uniform velocity inlet. The maximum variations in \overline{Nu} are around 0.7% and 0.9% with regard to the study by Chatterjee and Mondal [25] and Sharma and Eswaran [26], respectively. Again, an excellent agreement of present unconfined results exists with aforementioned studies [25, 26]. However, the deviations in C_D are found within approximately 5% of those in other studies [12, 28]. Strouhal number differs by $\sim 1.7\%$ and 0.3% from those in another study [12, 25] for $Re = 100$ and 150 , respectively. It is also valuable to state that the maximum variations of up to 5% are not at all unusual in the literature [32]. Furthermore, the present methodology is validated in our previous studies [1, 33]. Thus, the results found in the current work are in good agreement with the results existing in the literature and therefore can be deemed trustworthy.

4.2 Fluid flow characteristics

Flow patterns around a square obstacle for the working fluid as air ($Pr = 0.7$) can be found in a previous study [1] at $G = 0.25$ to 1, while for Re up to 100. Therefore, this section covers the flow features which are not been covered in the previous study [1]. The time-averaged streamlines are plotted for $Re = 100$ – 150 at $G = 0.25$ – 1 in figure 4. The twin vortices are formed at the rear of the square cylinder (figure 4c–4i) except for $Re < 150$ at $G = 0.25$. The channel wall has a small influence on the upper vortex of the twin vortices behind the square cylinder; however, the lower vortex is more stretched towards downstream than towards the upper vortex. The upper vortex is diminished/shortened on decreasing gap ratio (or increasing wall effect). At $G = 0.25$, a single time-averaged vortex is observed at the rear of the square obstacle up to $Re = 125$. In addition, a wake is formed on the downstream channel wall and its height increases laterally on decreasing gap ratio from 1 to 0.25. On increasing Re , this wake flattens along the channel wall and hence its size increases. The flow is observed to be steady for Re up to 121 at $G = 0.5$. The conversion to a time-periodic regime from a steady regime is presented in figure 5a–5b by providing the temporal variation of the lift coefficient. It can be noted that the onset of the shifting to a time-periodic regime from a steady regime exists at $Re = 122$ for $G = 0.5$. Also, as the gap ratio reduces the delay in the shifting of time-periodic regime from steady regime is observed. To demarcate the (periodic) unsteady regime at differing values of Re and G , numerical analysis has been performed in the complete

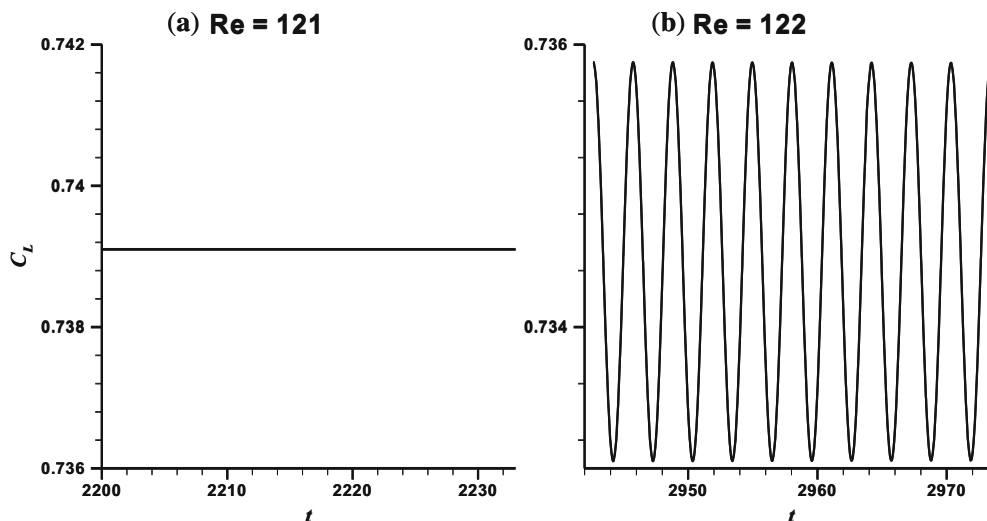


Figure 5. Onset of transition from a steady to a time-periodic regime: C_L vs t plot for $G = 0.5$.

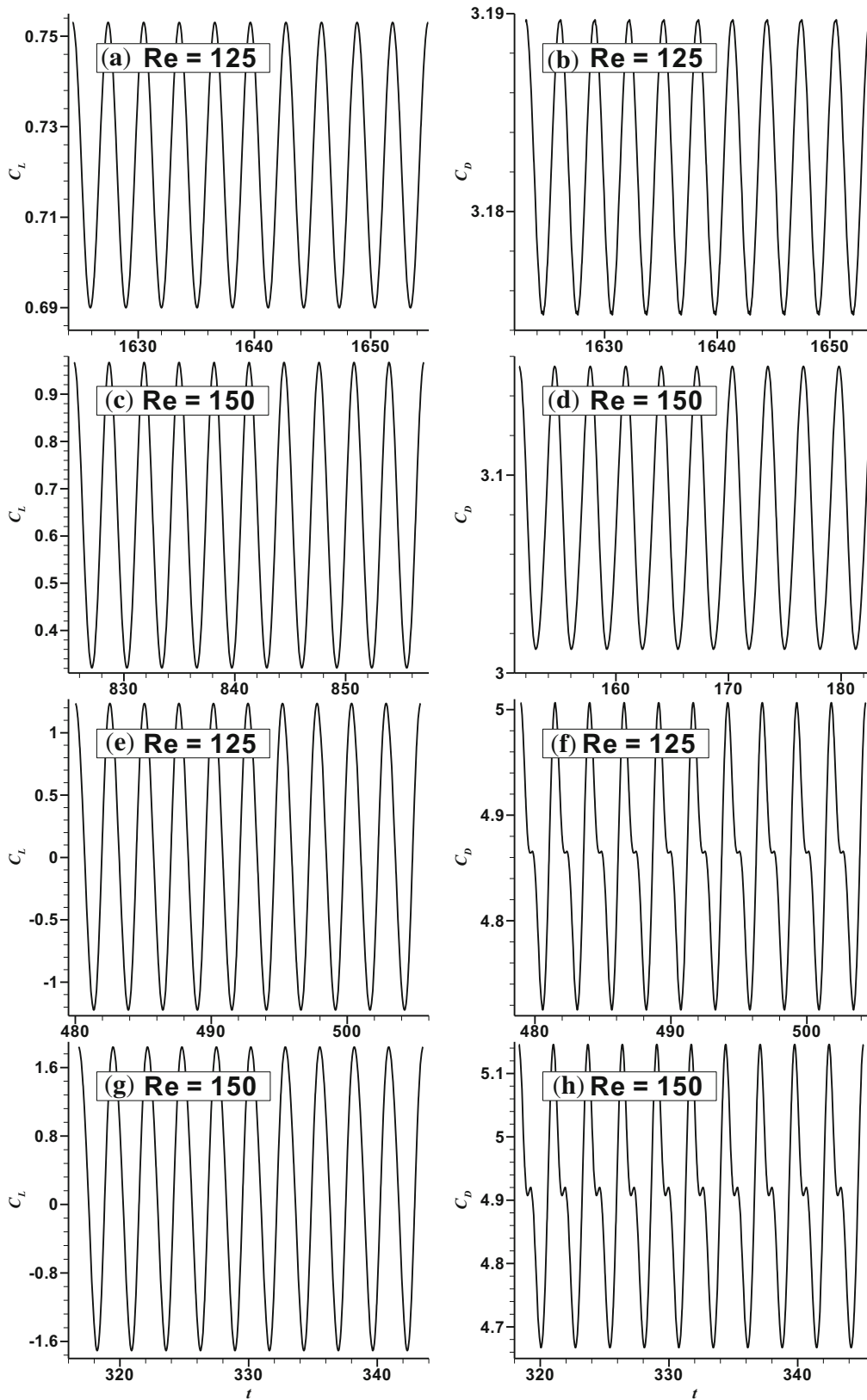


Figure 6. Time history of C_L and C_D for (a-d) $G = 0.5$ and (e-h) $G = 1$ at different values of Re .

domain and the frequency of the vortex shedding (Strouhal number) is recorded with time. It is also valuable to state that the transition to periodic unsteady regime occurs after $Re = 45$ for the free stream flow past a long square obstacle [34, 35]. Analogous to the transition of time-periodic regime from a steady regime, the flow separation from the surface of the square obstacle delays with decreasing gap ratio. An asymmetric vortex is observed downstream on the bottom wall of the square obstacle at $G = 0.25$ for $Re \leq 150$. Similarly, for

$G = 0.5$, an asymmetric vortex is formed at $Re \leq 100$ and at $G = 1$, an asymmetric vortex is found at $Re = 1$.

The variation of the time history of flow output parameters (drag and lift coefficients) is presented in figure 6 for $Re > 100$ at different G . In the unsteady time-periodic regime, full-domain computations are carried out until 10 cycles of almost constant amplitude are obtained for the output parameters. Moreover, these instantaneous values of the output parameters in 10 periodic cycles are employed to analyse their time-

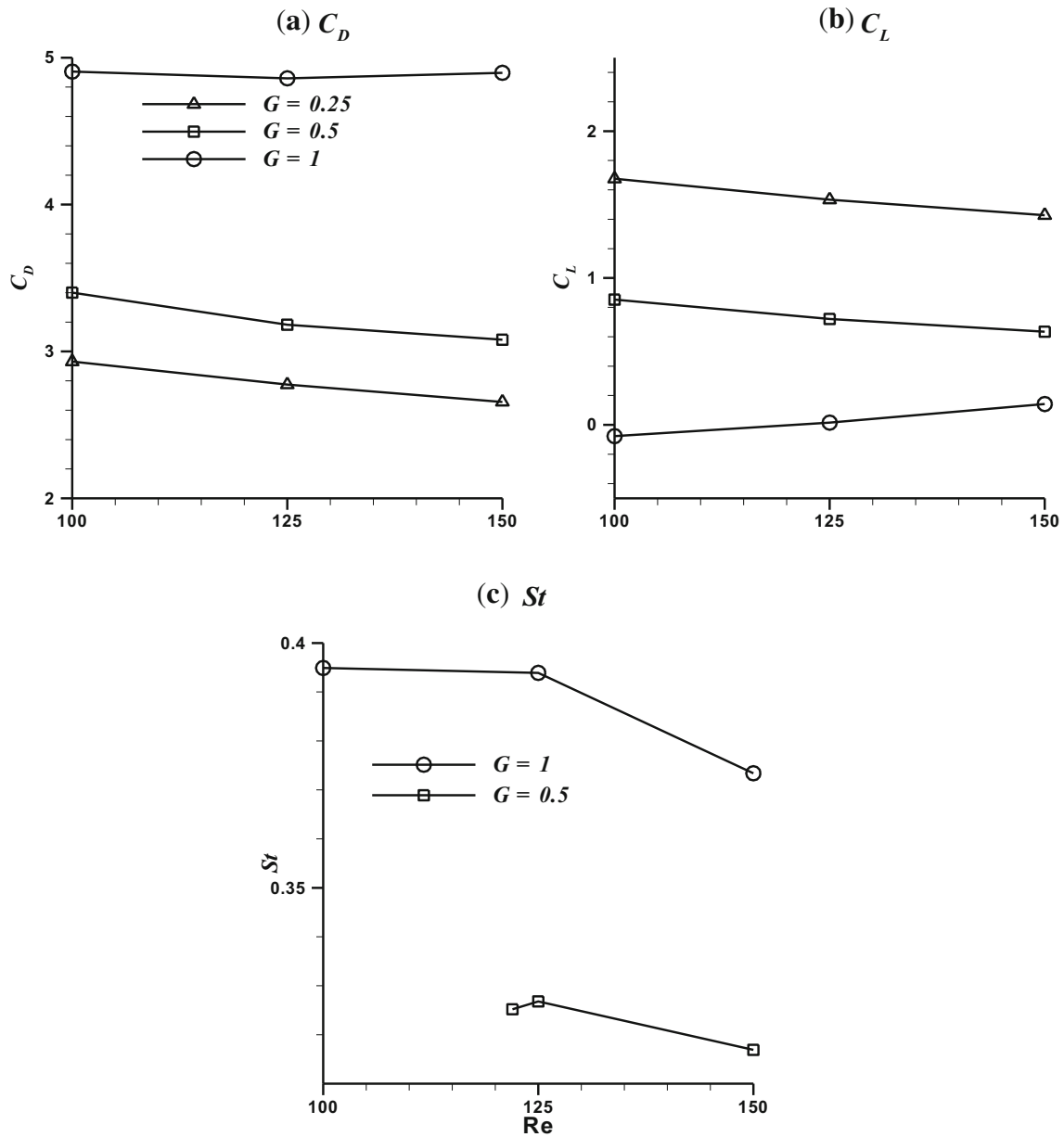


Figure 7. Variation of (a) C_D , (b) C_L and (c) St with Re and G .

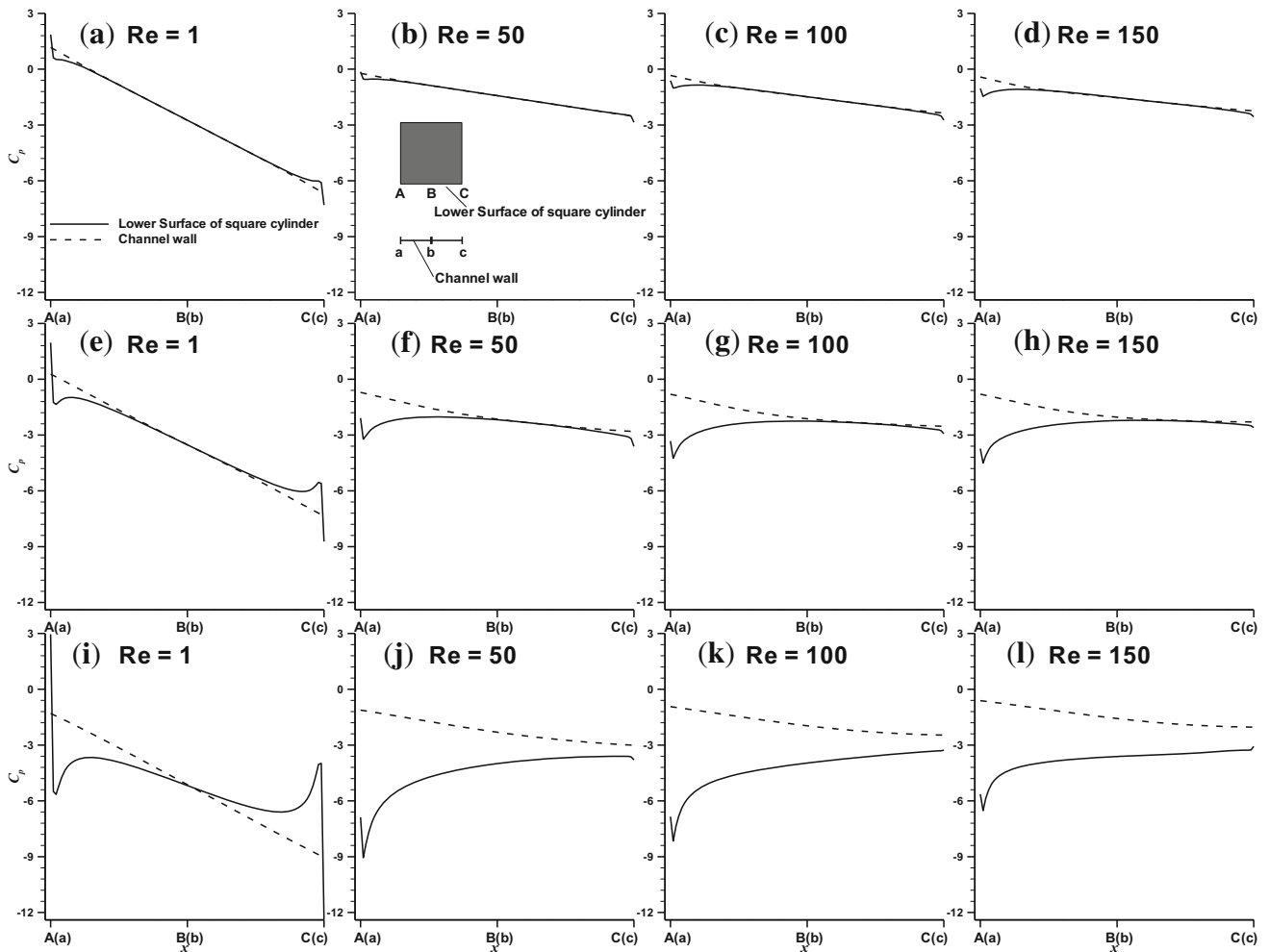


Figure 8. Pressure coefficient variation along the lower surface of the square cylinder and the channel wall for (a–d) $G = 0.25$, (e–h) $G = 0.5$ and (i–l) $G = 1$.

averaged values. The amplitudes of C_D and C_L increase with increase in Re and G (figure 6) because as the gap ratio increases the interaction between the lower domain wall shear layer and the shear layer of the bottom surface of the square obstacle decreases and hence the drag and lift forces are enhanced. At the same instance, the time period for a cycle increases with increase in Re , which implies that vortices are now shed with a lower frequency. However, the time period for a cycle lowers with increase in G , which implies that on going away from the wall the frequency of vortices is increasing. It is also found that the drag coefficient cycles appear with one additional pseudo peak for $G = 1$. The existence of two peaks in one complete time cycle is the outcome of the establishment and subsequent separation of vortices (vortex shedding) alternatively from either side of the square obstacle, that is, two rows of vortices are shed alternatively from

the bottom and top surfaces of the square obstacle for the given range of G [8].

Figure 7a shows the variation of overall drag coefficient for $Re \geq 100$ and $G = 0.25$ –1. The values of total drag coefficients show a decreasing non-linear dependence on Re for all gap spacings. Also, a simple heat transfer expression as developed in our recent work [1] can be employed to compute the in-between values of the overall drag coefficients even for the extended ranges of Re covered in this work. The deviation of the drag coefficient correlation [1] with respect to existing computed results is found to have a maximum of $\sim 10.4\%$ (at $Re = 5$), 6.3% (at $Re = 125$) and 9.3% (at $Re = 50$) for $G = 0.25$, 0.5 and 1 , respectively. The corresponding average deviations are $\sim 4.8\%$, 3.1% and 4.7% for $G = 0.25$, 0.5 and 1 , respectively.

Figure 7b presents the overall lift coefficient at $Re \geq 100$ and $G = 0.25$ –1. As observed in [1] at high Re , pressure at the top surface increases for $G = 0.25$ and 0.5

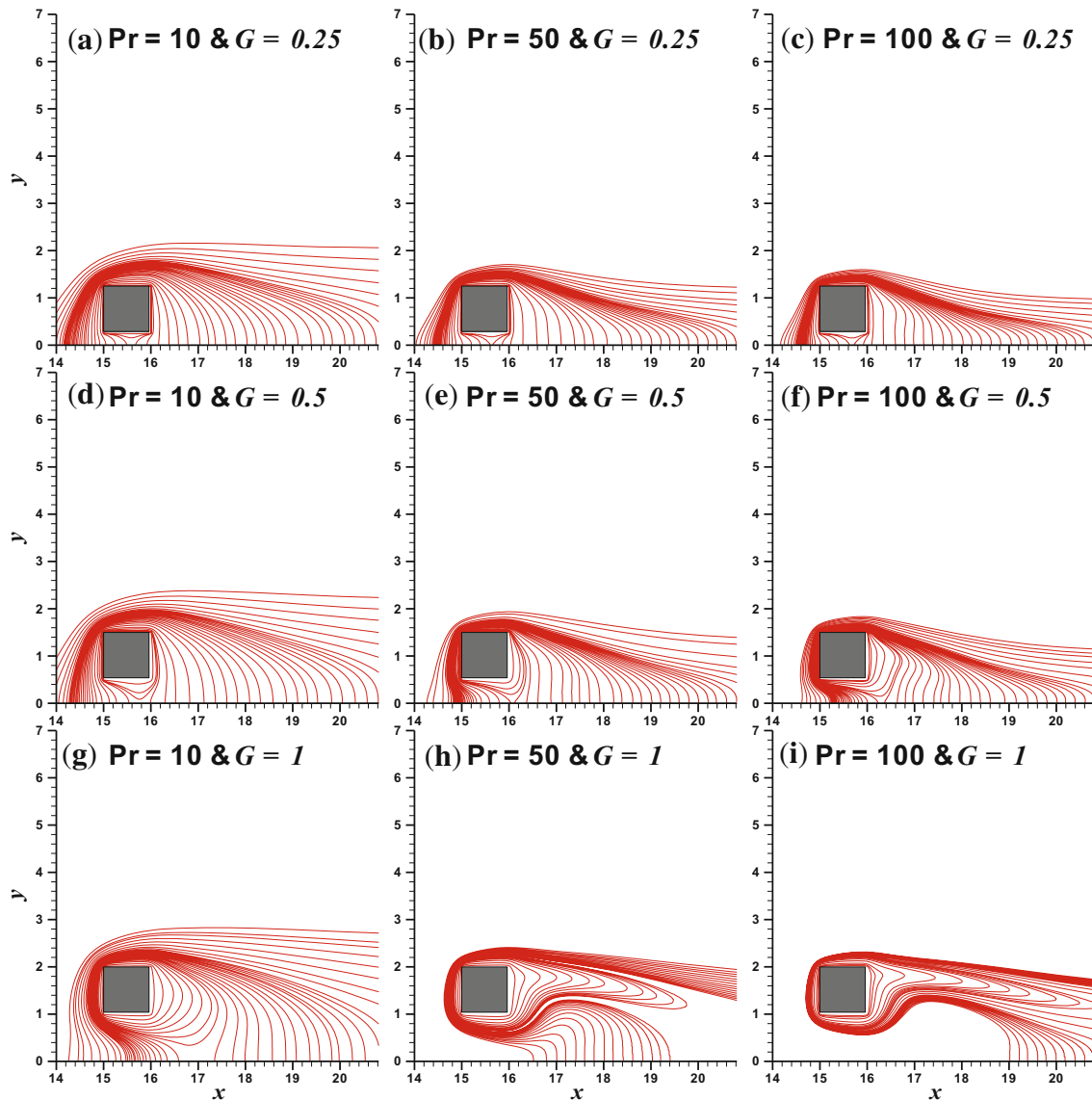


Figure 9. Isotherm contours around a square cylinder near a wall at different values of Pr and G for $Re = 1$.

with increase in Re but it decreases for $G = 1$. The difference between the bottom and top surface pressures contributed to lift coefficient. Hence, with increasing Re , lift coefficient decreases for $G = 0.25$ and 0.5 , and it increases for $G = 1$ (figure 7b). The Strouhal number values with Re (100–150) and G (0.25–1) are presented in figure 7c. It is found that the flow is time periodic for $Re \geq 122$ at $G = 0.5$. The value of the Strouhal number increases with the rise in gap ratio. This suggests that the wavering motion rises with rising gap ratio. It can also be noted from this figure that the maximum values of the Strouhal numbers appear at $Re = 100$ and 125 for $G = 1$ and 0.5 , respectively. As expected, the Strouhal number for the current flow system is higher than that for the unconfined square obstacle [13, 34, 35].

Furthermore, the pressure distribution on the lower surface of the square cylinder and the channel wall is presented to explore the effect of changing G and Re . The difference in pressure coefficient between the lower surface of the square cylinder and the channel wall (that is, in the gap region) is almost negligible at $G = 0.25$ (figure 8a–8d). Similarly, for $G = 0.5$, the difference in pressure coefficient is almost negligible at the core (at Bb) of the gap region and also negligible on moving from Bb to Cc (figure 8e–8h). At $G = 1$, the core of the gap region has a negligible pressure coefficient difference for $Re = 1$ (figure 8i). This shows that for gap ratios (0.25–0.5) and/or $Re = 1$, the gap region flow is unidirectional, and the core flow looks like the channel flow. This observation is also consistent with the

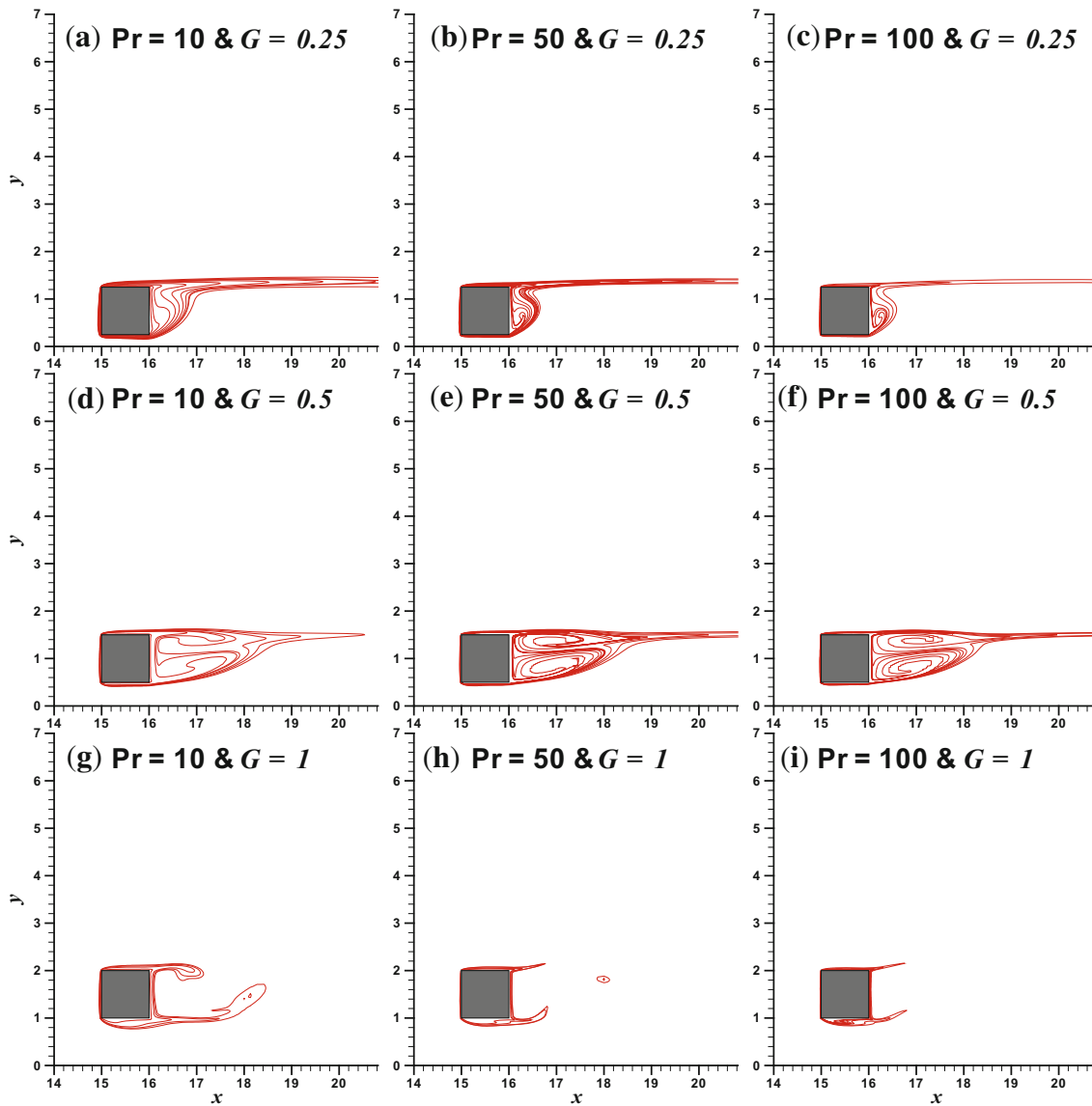


Figure 10. Isotherm contours around a square cylinder near a wall at different values of Pr and G for $Re = 100$.

experimental and numerical findings reported in [21] and [13], respectively. On the other hand, significant change in pressure coefficient difference can be noted at $G = 1$. Also, the pressure coefficient distribution on the lower surface of the square cylinder is less than that on the channel wall for $Re > 1$ at $G = 1$ (figure 8j–l).

4.3 Thermal characteristics

The temperature fields close to the wall near the square obstacle are given by isotherm contours for $Pr = 10, 50$ and 100 in figures 9a–9i, 10a–10i and 11a–11i for $Re = 1, 100$ and 150 at $G = 0.25, 0.5$ and 1 , respectively. Similar to results at $Pr = 0.7$ [1], presence of the adiabatic wall causes an asymmetry in the temperature fields near the obstacle.

Figures 9, 10 and 11 show that on increasing Re , the hydrodynamic boundary layer decreases, and also with increasing Pr the thermal boundary layer decreases [36]. It is also consistent with the growing values of the gap ratio at a constant Re and Pr . Figure 9 shows that due to low Re , heat transfer is interrupted by the presence of a channel wall. Hence, the temperature difference between the channel wall and the square obstacle is low. This difference in temperature increases with increasing G and/or Pr due to shrinking of isotherms. Hence, the thermal boundary layer reduces with the increase in gap ratio. Also, the temperature difference between the channel wall and the square obstacle is reduced with increasing Re .

The longitudinal span of the recirculation region after the square obstacle enhances with growing Re and also the

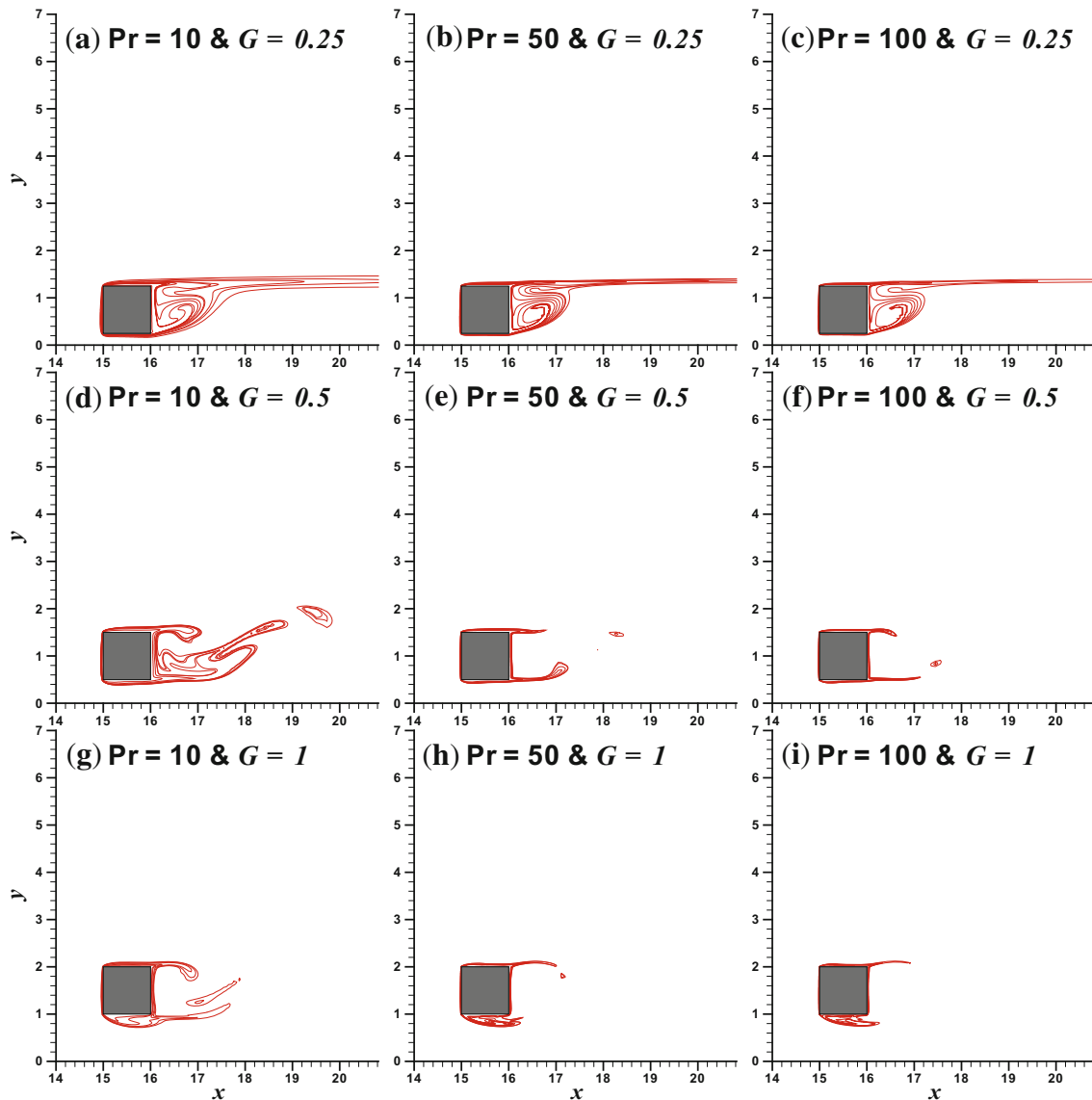


Figure 11. Isotherm contours around a square cylinder near a wall at different values of Pr and G for $Re = 150$.

congestion of the thermal contours close to the back surface of the square obstacle increases (figures 9, 10, 11). The effective heat transfer area with the bottom wall of the square cylinder decreases with increasing G and also the wall interruption is reduced. On increasing Pr , the thermal boundary layer becomes weaker and hence the crowding of the temperature contours near the square cylinder increases (figures 9, 10, 11). The isotherms around the square cylinder also extend axially with increasing Pr .

The time history of heat transfer output parameter (Nusselt number) is generated and shown in figure 12 at $Pr = 10, 100$ for $Re = 125, 150$ and $G = 0.5, 1$. The amplitude of average Nusselt number increases with G . Also, it increases with Re except at $G = 1$ for $Pr \geq 50$. The mixed trend is observed with increasing Pr . The local

maximum is observed at $Pr = 50$ for $G = 0.5$. At $G = 1$, the local minimum is found at $Pr = 50$ for $Re = 125$ and it decreases monotonically with Pr for $Re = 150$. Similar to the flow output parameters, the time period for a cycle improves with increasing Re and deteriorates with increasing G . For higher Re , Pr and G (that is, $Re = 150$, $Pr = 100$ and $G = 1$), the Nusselt number cycles also have one additional pseudo peak (figure 12h).

The average surface Nusselt number on the surfaces of the square bar in the steady regime for $Pr \geq 10$ at various values of Re and G is presented in figure 13a–13d. The local Nusselt number (Nu) at this juncture is described as $-\partial\theta/\partial n$. The average surface value on each face of the square body is computed by taking the average of the local values. In general, for an unconfined square obstacle,

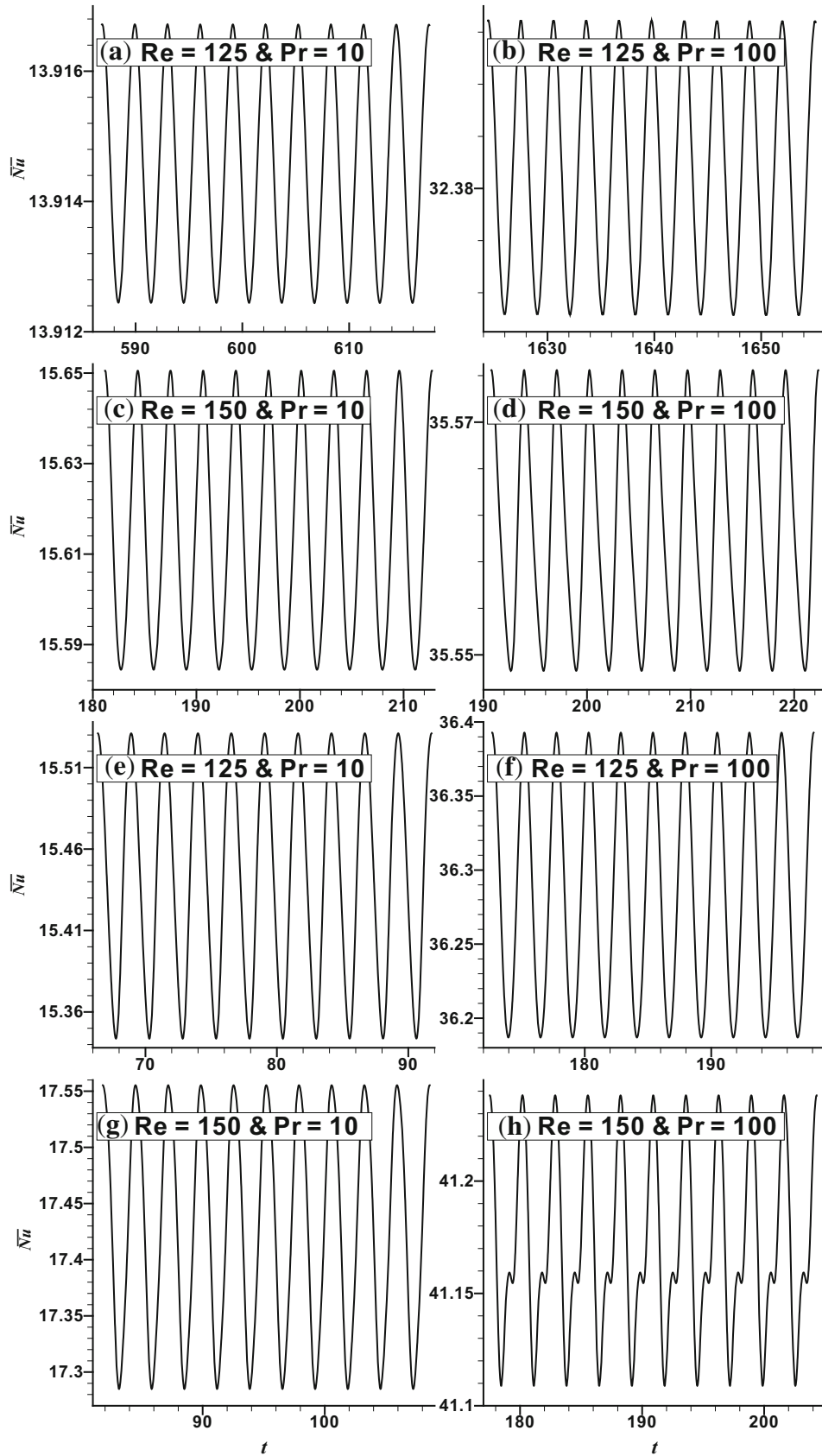


Figure 12. Time history of Nusselt number for (a-d) $G = 0.5$ and (e-h) $G = 1$ at different values of Re , Pr .

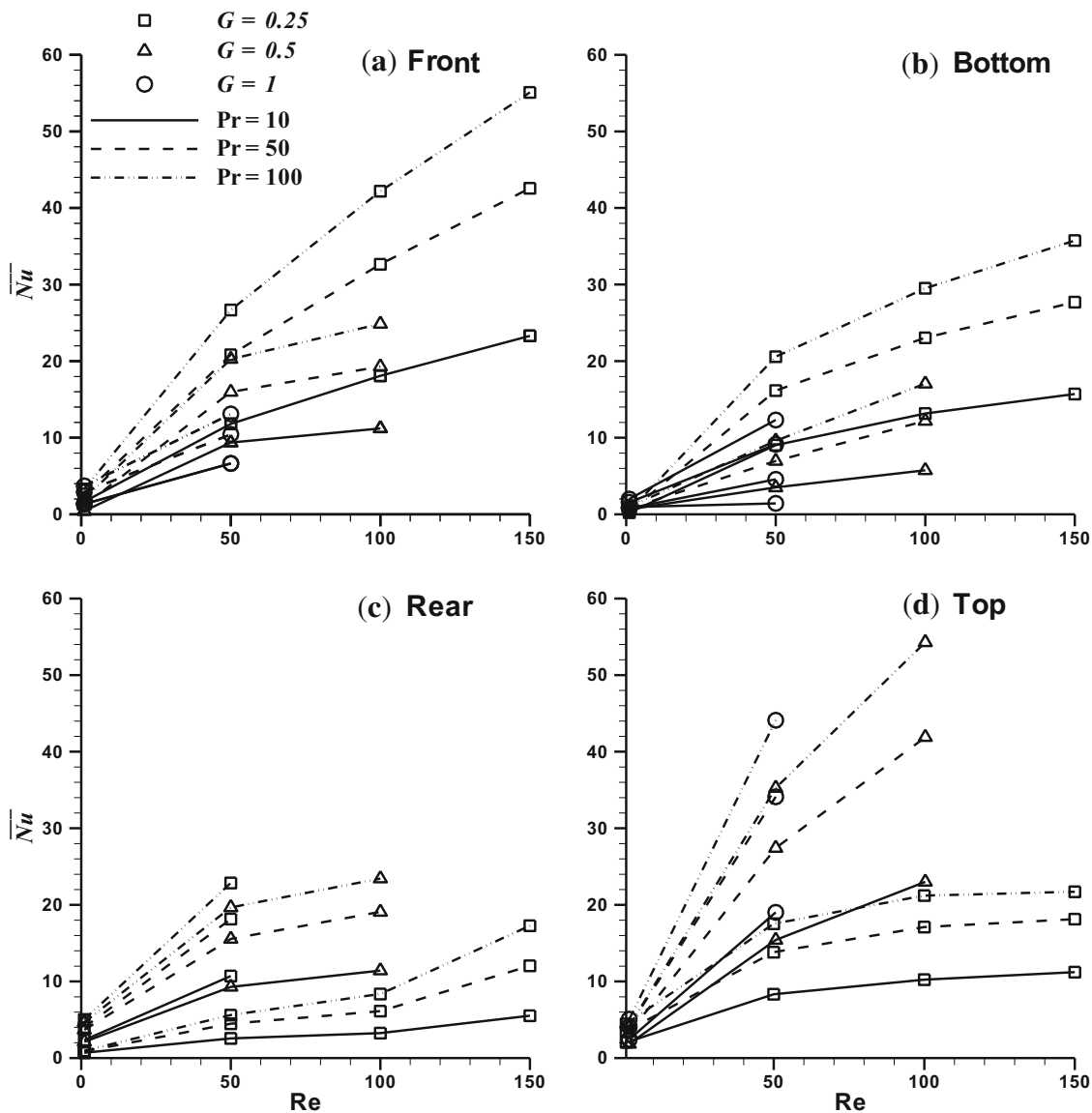


Figure 13. Variation of average Nusselt number of (a) front, (b) bottom, (c) rear and (d) top surfaces of 2-D square cylinder near a wall with Re , Pr and G in the steady regime.

the front surface has the maximum Nusselt number, while the back surface has the least value of Nusselt number and the bottom and top surfaces have the same Nusselt number values [35]. For the occurrence of a square obstacle near a moving wall with uniform inlet velocity, the maximum and the minimum heat transfer rates appear along the front and back faces, respectively. The presence of a moving wall decreases the heat transfer rate along the top surface with decreasing G [15]. In linear inlet velocity, the velocity increases on moving from the bottom to the top. At low Re , the wall acts as a stationary wall and interrupts the heat transfer. Hence, the highest and the least Nusselt number values are observed on the top and

bottom surfaces, respectively (figure 13). Similar results are obtained for higher gap ratio ($G = 1$) because at high gap ratio velocity difference plays the major role. On increasing Re , the near-wall fluid acts as a moving wall for a low gap ratio ($G = 0.25$). Hence, the similar results of a moving wall [15] are obtained. It is observed from figure 13 that as Pr and/or Re increases the heat transfer enhances for all the surfaces.

The average cylinder Nusselt number (\overline{Nu}) values for different Pr (≥ 10) with Re and G are shown in figure 14. The \overline{Nu} values are achieved by taking the mean of the average Nusselt number values on the faces. With

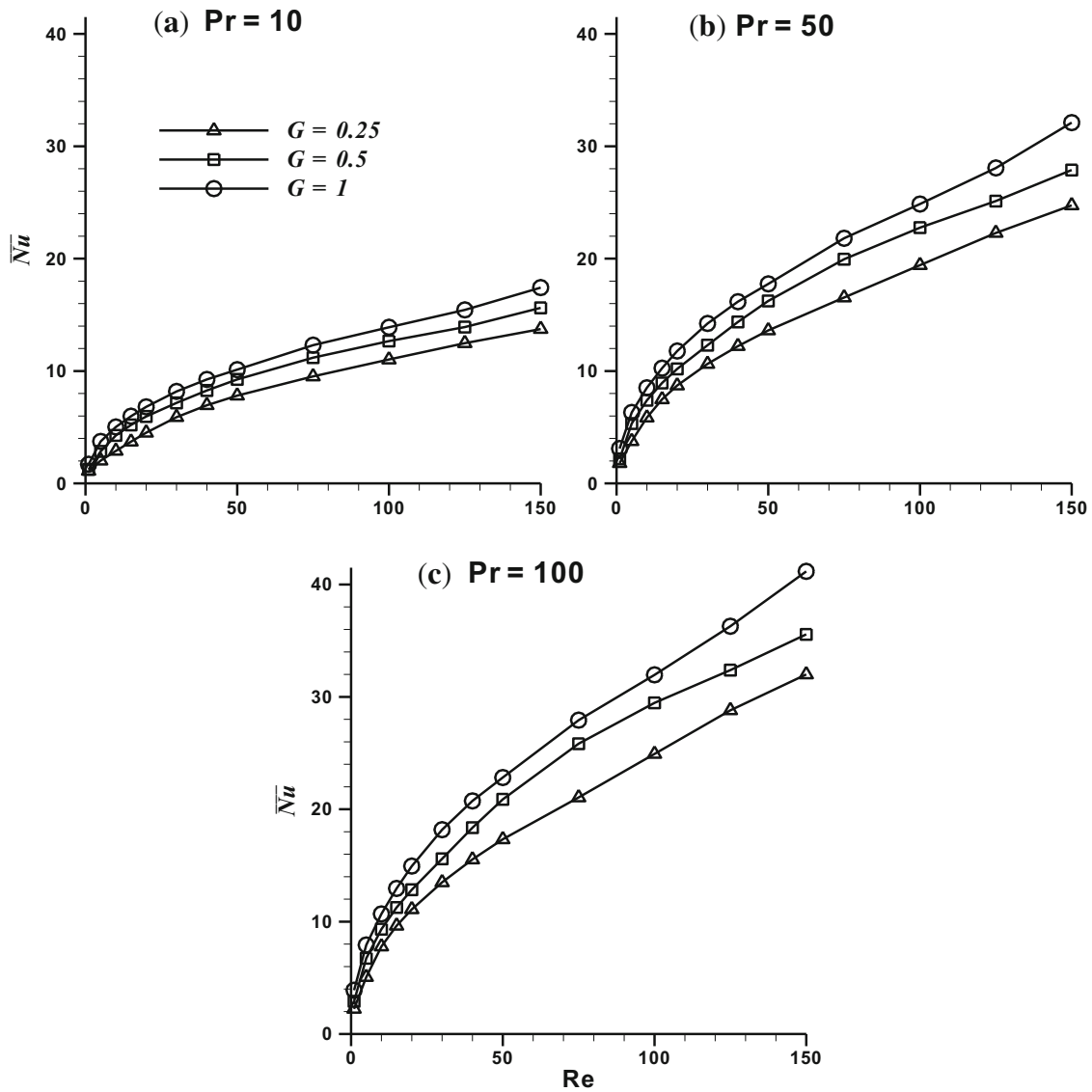


Figure 14. Variation of the \overline{Nu} with Re and G for (a) $Pr = 10$, (b) $Pr = 50$ and (c) $Pr = 100$.

increasing gap height, heat transfer on the front face reduces and the opposite trends are observed on the back and top surfaces; whereas a mixed trend is found on the bottom surface [1]. However, from isotherm contours, wall interruption reduces with increasing G and also the congestion of isotherms mainly in the back surface enhances with increasing G . So, the rear face increase in average Nusselt number is much higher than the decrease caused by the front surface. Hence, the \overline{Nu} values increase with the increase in G . Also, the average cylinder Nusselt number rises with the rise in Pr and/or Re as the surface average Nusselt number rises with the increase in Pr and/or Re . The disparity among the values of an average cylinder Nusselt number also increases with increasing G for constant values of Re and Pr .

The heat transfer enhancement is computed for various Re , Pr and G . The enhancement in the \overline{Nu} values for various Pr with respect to $Pr = 0.7$ is given in figure 15a–15c. Similarly, figure 15d–15f provides the enhancement in the \overline{Nu} for different gap ratios against $G = 0.25$. The heat transfer enhancement increases with the rise in Pr (figure 15a–15c) and G (figure 15d–15g) at any Re . The maximum increase in heat transfer attained is $\sim 660\%$ (at $Re = 30$, $Pr = 100$ and $G = 0.25$) against the analogous values at $Pr = 0.7$, $\sim 89\%$ (at $Re = 20$, $Pr = 0.7$ and $G = 1$) against the equivalent values at $G = 0.25$ and $\sim 1332\%$ (at $Re = 150$, $Pr = 100$ and $G = 0.25$) against the corresponding values at $Re = 1$.

Furthermore, the Colburn heat transfer factor (j_h) is presented with Re , G and Pr in figure 16a–16c, which is

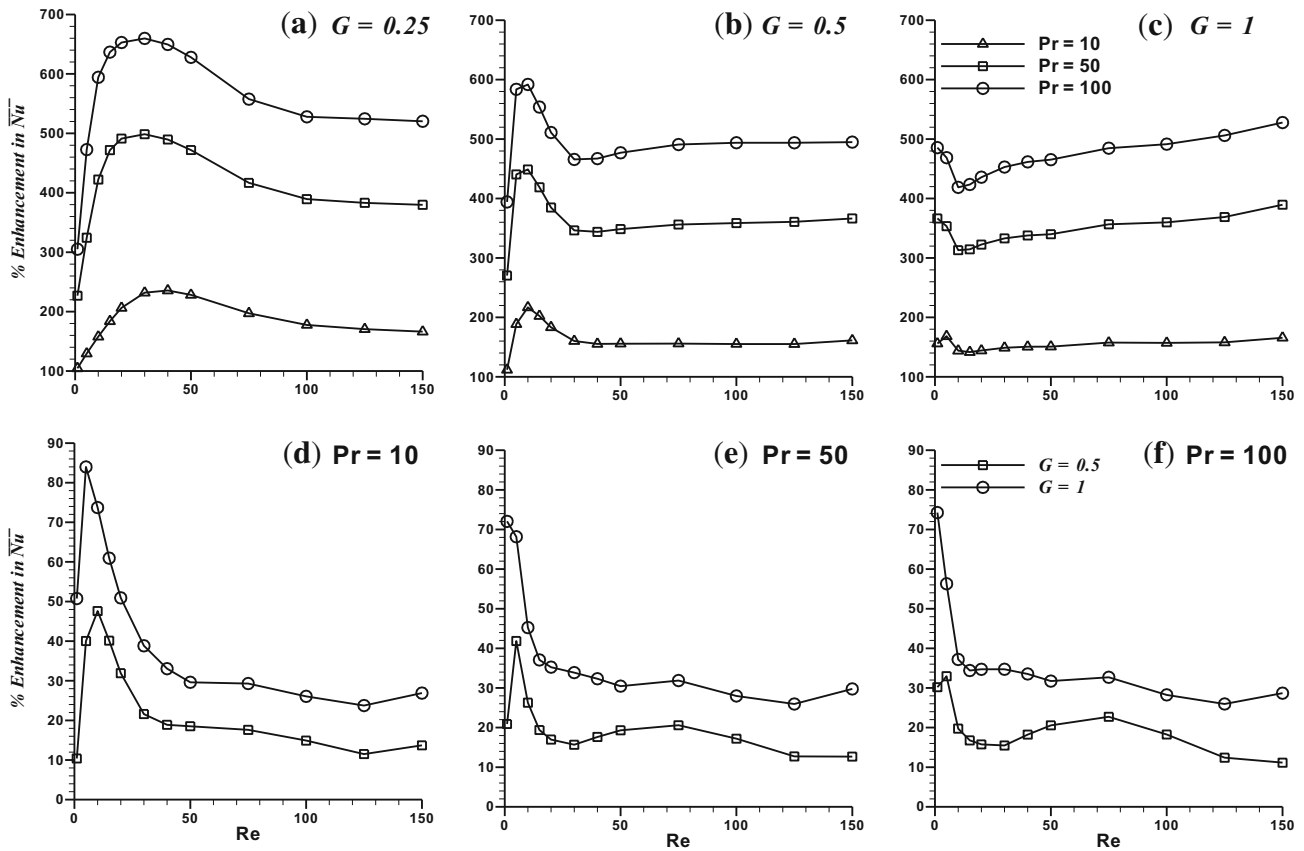


Figure 15. Percent enhancement in \overline{Nu} with Re for (a–c) different Prandtl numbers with respect to $Pr = 0.7$ at $G = 0.25$ – 1 and (d–f) different gap ratios with respect to $G = 0.25$ at $Pr = 10$ – 100 .

described as $j_h = \overline{Nu}/(Re Pr^{1/3})$. It is notable from this figure that with rising G , the j_h factor enhances; however, these results are more notorious at low Re . The j_h factor increases with rising Pr . It is also valuable to note that all the values of the j_h factor more or less coincide onto a single curve at different values of Re and G for $Pr = 10$ – 100 . So, a heat transfer correlation (Eq. 5) is formulated for the given Pr range ($Pr \geq 10$) at different values of Re and G covered. Based on the earlier studies [1, 33, 36, 37], this correlation is generated by applying best fit method. Also, the flow is dominated by viscous diffusion for $Pr > 0.7$; however, at $Pr = 0.7$, flow is dominated by thermal diffusion [1].

$$j_h = 0.721G^{0.288}Re^{-0.5} \quad (5)$$

This correlation has the upper limit deviation of $\sim 14.7\%$ (at $Re = 5$, $Pr = 10$ and $G = 0.25$) and the mean deviation of $\sim 5.7\%$ with present computed values.

5. Conclusions

Forced convection heat transfer from a square obstacle in the neighbourhood of a wall is studied in a horizontal plane for $1 \leq Re \leq 150$, $10 \leq Pr \leq 100$ and $0.25 \leq G \leq 1$. The key points of this study are as follows:

- The numerical methodology has been validated extensively.
- The fluid flow and heat transfer fields remain steady for $G = 0.5$ up to $Re = 121$. Thus, the onset of time-periodic regime is originated at $Re = 122$ for $G = 0.5$.
- In time-periodic regime, the peak amplitudes of average Nusselt number, drag and lift coefficients increase with rise in G .
- The \overline{Nu} and the j_h factor are observed to rise with increasing Pr .
- The average surface Nusselt number along the front surface of the square cylinder rises gradually with increase in gap ratio and the opposite scenario is obtained for the top and rear surfaces.
- Maximum rise in heat transfer is obtained approximately 1332% at $Re = 150$ ($Pr = 100$, $G = 0.25$) against the analogous values at $Re = 1$.
- Finally, the correlation of the Colburn j_h factor has been established for the ranges covered. Also, it has been ensured that the drag coefficient correlation developed in [1] can be utilised even for the extended ranges of Re .

Investigation of forced convection heat transfer for non-Newtonian fluids would be the scope for future study at low Re for varying G and Pr .

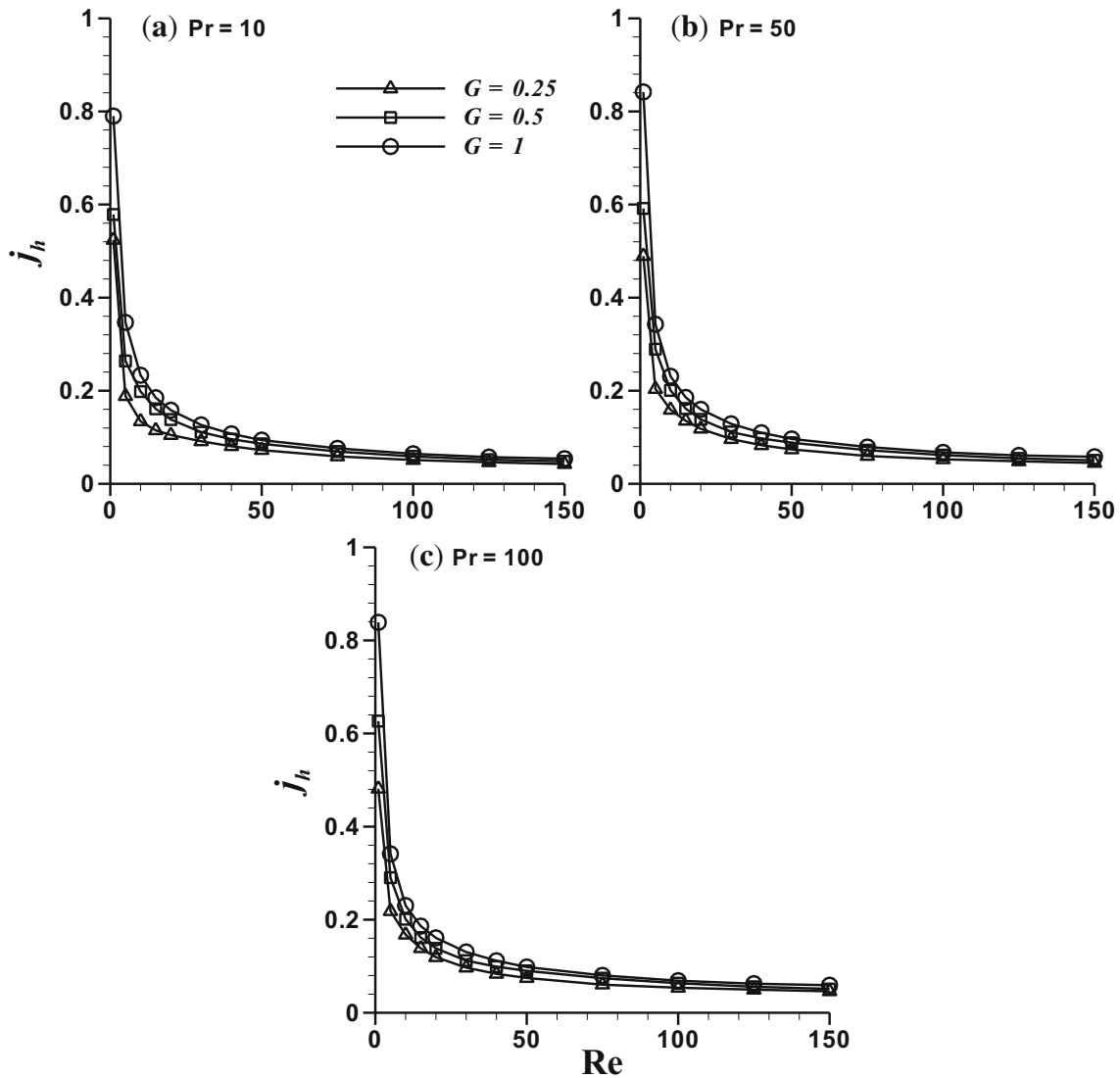


Figure 16. Variation of the j_h factor with Re and G for (a) $Pr = 10$, (b) $Pr = 50$ and (c) $Pr = 100$.

Acknowledgements

Authors would like to thank two anonymous reviewers for their valuable suggestions on this work.

Notations

C_D	drag coefficient $\left(\frac{2F_D}{\rho U_\infty^2 D}\right)$
C_L	lift coefficient $\left(\frac{2F_L}{\rho U_\infty^2 D}\right)$
C_p	pressure coefficient $\left(\frac{2\Delta p}{\rho U_\infty^2}\right)$
c_p	specific heat (J/kg.K)
CV	control volume
D	side of the square obstacle (m)
F_D	drag force (N/m)

F_L	lift force (N/m)
f	frequency of vortex shedding (1/s)
G	gap ratio $\left(\frac{G^*}{D}\right)$
H	domain height (m)
h	coefficient of local heat transfer (W/m ² K)
\bar{h}	coefficient of average heat transfer (W/m ² K)
j_h	Colburn factor of heat transfer
k	thermal conductivity (W/m K)
L_d, L_u	downstream and upstream distances, respectively (m)
n	normal direction
N	control volumes on a side of the square obstacle
Nu	local Nusselt number $\left(\frac{hD}{k}\right)$
\bar{Nu}	average Nusselt number $\left(\frac{\bar{h}D}{k}\right)$
p	pressure $\left(\frac{p^*}{\rho U_\infty^2}\right)$

Pr	Prandtl number $\left(\frac{\mu c_p}{k}\right)$
Re	Reynolds number $\left(\frac{DU_\infty \rho}{\mu}\right)$
St	Strouhal number $\left(\frac{fD}{U_\infty}\right)$
t	time $\left(\frac{t^*}{\left(\frac{D}{U_\infty}\right)}\right)$
T	temperature (K)
T_∞	inlet fluid temperature (K)
T_w	square obstacle temperature (K)
U_∞	inlet fluid average velocity (m/s)
u^*, v^*	components of velocity in x^* and y^* directions, respectively (m/s)
x^*, y^*	axial and lateral coordinates respectively (m)

Greek symbols

ρ	fluid density (kg/m ³)
μ	dynamic viscosity (Pa.s)
δ	smallest cell size (m)
θ	dimensionless temperature $\left(\frac{T-T_\infty}{T_w-T_\infty}\right)$

Superscript

* dimensional value

References

- [1] Kumar D and Dhiman A 2016 Computations of Newtonian fluid flow around a square cylinder near an adiabatic wall at low and intermediate Reynolds numbers: effects of cross-buoyancy mixed convection. *Numer. Heat Transf. Part A* 70: 162–186
- [2] Lei C, Cheng L, Armfield S W and Kavanagh K 2000 Vortex shedding suppression for flow over a circular cylinder near a plane boundary. *Ocean Eng.* 27: 1109–1127
- [3] Zovatto L and Pedrizzetti G 2001 Flow about a circular cylinder between parallel walls. *J. Fluid Mech.* 440: 1–25
- [4] Shi J M, Breuer M and Durst F 2002 Wall effect on heat transfer from a micro-cylinder in near-wall shear flow. *Int. J. Heat Mass Transf.* 45: 1309–1320
- [5] Reichl P, Hourigan K and Thompson M C 1998 Flow past a cylinder submerged under a free surface. *13th Australasian Fluid Mechanics Conference*, pp. 943–946
- [6] Reichl P, Hourigan K and Thompson M C 2003 The unsteady wake of a circular cylinder near a free surface. *Flow Turbul. Combust.* 71: 347–359
- [7] Reichl P, Hourigan K and Thompson M C 2005 Flow past a cylinder close to a free surface. *J. Fluid Mech.* 533: 269–296
- [8] Singha A K, Sarkar A and De P K 2008 Numerical study on heat transfer and fluid flow past a circular cylinder in the vicinity of a plane wall. *Numer. Heat Transf. Part A* 53: 641–666
- [9] Cheng M and Luo L S 2007 Characteristics of two-dimensional flow around a rotating circular cylinder near a plane wall. *Phys. Fluids* 19: 063601–0636018
- [10] Rao A, Stewart B E, Thompson M C, Leweke T and Hourigan K 2011 Flows past rotating cylinders next to a wall. *J. Fluids Struct.* 27: 668–679
- [11] Sarkar S and Sarkar S 2010 Vortex dynamics of a cylinder wake in proximity to a wall. *J. Fluids Struct.* 26: 19–40
- [12] Bhattacharyya S and Maiti D K 2004 Shear flow past a square cylinder near a wall. *Int. J. Eng. Sci.* 42: 2119–2134
- [13] Bhattacharyya S and Maiti D K 2006 Vortex shedding suppression for laminar flow past a square cylinder near a plane wall: a two-dimensional analysis. *Acta Mech.* 184: 15–31
- [14] Bhattacharyya S, Maiti D K and Dhinakaran S 2006 Influence of buoyancy on vortex shedding and heat transfer from a square cylinder in proximity to a wall. *Numer. Heat Transf. Part A* 50: 585–606
- [15] Dhinakaran S 2011 Heat transport from a bluff body near a moving wall at $Re = 100$. *Int. J. Heat Mass Transf.* 54: 5444–5458
- [16] Mahir N 2009 Three-dimensional flow around a square cylinder near a wall. *Ocean Eng.* 36: 357–367
- [17] Harichandan A B and Roy A 2012 Numerical investigation of flow past single and tandem cylindrical bodies in the vicinity of a plane wall. *J. Fluids Struct.* 33: 19–43
- [18] Ryu K, Yook S J and Lee K S 2014 Forced convection across a locally heated square cylinder near a wall. *Numer. Heat Transf. Part A* 65: 972–986
- [19] Bosch G and Rodi W 1996 Simulation of vortex shedding past a square cylinder near a wall. *Int. J. Heat Fluid Flow* 17: 267–275
- [20] Bosch G, Kappler M and Rodi W 1996 Experiments on the flow past a square cylinder placed near a wall. *Exp. Therm. Fluid Sci.* 13: 292–305
- [21] Martinuzzi R J, Bailey S C C and Kopp G A 2003 Influence of wall proximity on vortex shedding from a square cylinder. *Exp. Fluids* 34: 585–596
- [22] Wang X K and Tan S K 2008 Comparison of flow patterns in the near wake of a circular cylinder and a square cylinder placed near a plane wall. *Ocean Eng.* 35: 458–472
- [23] Shi L L, Liu Y Z and Sung H J 2010 On the wake with and without vortex shedding suppression behind a two-dimensional square cylinder in proximity to a plane wall. *J. Wind Eng. Ind. Aerodyn.* 98: 492–503
- [24] Shi L L, Liu Y Z and Sung H J 2010 Influence of wall proximity on characteristics of wake behind a square cylinder: PIV measurements and POD analysis. *Exp. Therm. Fluid Sci.* 34: 28–36
- [25] Chatterjee D and Mondal B 2012 Effect of thermal buoyancy on the two-dimensional upward flow and heat transfer around a square cylinder. *Heat Transf. Eng.* 33: 1063–1074
- [26] Sharma A and Eswaran V 2005 Effect of channel-confinement and aiding/opposing buoyancy on the two-dimensional laminar flow and heat transfer across a square cylinder. *Int. J. Heat Mass Transf.* 48: 5310–5322
- [27] Davis R W and Moore E F 1982 A numerical study of vortex shedding from rectangles. *J. Fluid Mech.* 116: 475–506
- [28] Franke R and Rodi W 1990 Numerical calculation of laminar vortex shedding flow past cylinders. *J. Wind Eng. Ind. Aerodyn.* 35: 237–257

- [29] Treidler E B 1991 *An experimental and numerical investigation of flow past ribs in channel*. Ph.D. Thesis, University of California at Berkeley, CA
- [30] Kothandaraman C P and Subramanyan S 2014 *Heat and mass transfer data book*. New Delhi: New Age International
- [31] *ANSYS User Manual* 2009 Ansys, Inc., Canonsburg, PA
- [32] Roache P J 1998 *Verification and validation in computational science and engineering*. Albuquerque, New Mexico: Hermosa
- [33] Kumar D and Dhiman A 2016 Opposing buoyancy characteristics of Newtonian fluid flow around a confined square cylinder at low and moderate Reynolds numbers. *Numer. Heat Transf. Part A* 69: 874–897
- [34] Dhiman A K, Chhabra R P and Eswaran V 2006 Steady flow of power-law fluids across a square cylinder. *Chem. Eng. Res. Des.* 84: 300–310
- [35] Dhiman A K, Chhabra R P, Sharma A and Eswaran V 2006 Effects of Reynolds and Prandtl numbers on heat transfer across a square cylinder in the steady flow regime. *Numer. Heat Transf. Part A* 49: 717–731
- [36] Dhiman A K, Chhabra R P and Eswaran V 2005 Flow and heat transfer across a confined square cylinder in the steady flow regime: effect of Peclet number. *Int. J. Heat Mass Transf.* 48: 4598–4614
- [37] Dhiman A, Sharma N and Kumar S 2014 Buoyancy-aided momentum and heat transfer in a vertical channel with a built-in square cylinder. *Int. J. Sustain. Energy* 33: 963–984